Applied Physics B (2018) 124:72
https://doi.org/10.1007/s00340-018-6943-8

Applied Physics B
Lasers and Optics

Large astigmatic laser cavity modes and astigmatic compensation

T. D. Huang[1] · T. H. Lu[1]

Received: 2 January 2018 / Accepted: 2 April 2018

Abstract
In this paper, it was experimentally verified that anisotropic (astigmatic) Hermite–Gaussian modes can be generated from a hemi-cylindrical cavity and can be transformed into Laguerre–Gaussian modes by using an extra-cavity plano-convex cylindrical lens which can modify different beam divergence angle in the x–z and y–z planes. By controlling the off-axis pumping and the angle of the extra-cavity cylindrical lens, a variation in laser patterns was observed. Moreover, several additional relationships under different conditions have been analyzed. All experimental results corresponding to the theoretical analysis, and the role of the hemi-cylindrical cavity can be completely understood by comparing the theoretical and experimental results.

1 Introduction

The Laguerre–Gaussian (LG) laser mode, a helical-phase light beam, is a solution to the scalar Helmholtz equation under the paraxial approximation. The azimuthal phase term indicates that the optical angular momentum is carried by LG modes, and the optical vortices are defined as the phase singularity within the helical-phase light beam [1]. This method has attracted considerable attention in the studies of optical tweezers [2, 3], optical communication [4], optical testing [5], and quantum entanglement [6]. LG modes can be generated using several mode converters including cylindrical lenses [7, 8], a spiral phase plate [9], a q-plate [10], computer-generated holograms [11], and a spatial light modulator [12]. Moreover, it can be generated using a novel laser cavity [13, 14].

Large astigmatism can be induced by the hemi-cylindrical cavity which leads to the generation of anisotropic Hermite–Gaussian (HG) modes with different aspect ratios under propagation. In this paper, an extra-cavity plano-convex cylindrical lens was employed to modify the beam divergence angle and transform the incoming HG modes into LG modes. It was found that the beam divergence angle is a crucial parameter because all the experimental laser modes are affected by the relationship between the beam divergence angles of the horizontal and vertical directions.

Furthermore, this study has experimentally and theoretically extended the previous work [15] which only focuses on the transformation of laser patterns with the hemi-cylindrical cavity and extra-cavity cylindrical lens. We add more explanations and extended experiments. For example, to make the relationship between the beam divergence and the experimental results easier to understand, a quantitative analysis of the spot size in the x–z (horizontal direction) and y–z (vertical direction) planes, which verifies the experimental laser transverse mode that was generated from a hemi-cylindrical cavity with or without an extra-cavity cylindrical lens, was utilized. Finally, the relationships between the order of laser mode, the laser power, and the cavity length, as well as the relationship between the cavity length and the angle of the extra-cavity cylindrical lens, were further demonstrated. The hemi-cylindrical cavity with the extra-cavity cylindrical lens can be fully comprehended by comparing this study with the previous work.

2 Fundamental laser modes generated from a hemi-cylindrical cavity with or without an extra-cavity cylindrical lens

Diode pump laser cavities are composed of a cylindrical mirror, a flat mirror, and a gain medium within the hemi-cylindrical cavity. The hemi-cylindrical cavity can generate astigmatic HG or LG modes with an extra-cavity cylindrical lens. Figure 1 shows the composition of a hemi-cylindrical cavity. The pump source was an 808-nm fiber-coupled diode laser with a core diameter of 105 μm and a maximum power of 8 W. The focusing lens, which had a 38 mm focal length was used to lead the pump beam to

✉ T. H. Lu
thlu@ntnu.edu.tw

[1] Department of Physics, National Taiwan Normal University, Taipei, Taiwan

Published online: 05 April 2018

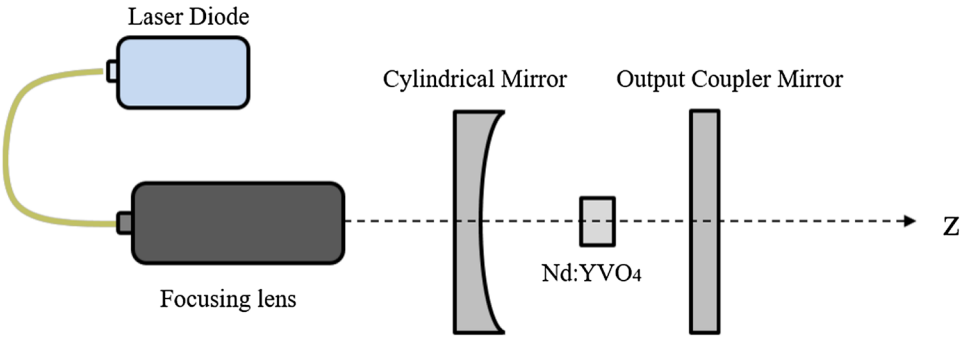

Fig. 1 Experimental setup of hemi-cylindrical cavity

the gain medium. A cylindrical concave mirror with a curvature radius (R) of 30 mm was employed as the front mirror; its reflectivity was 99% at 1064 nm. A flat mirror with 99% reflectivity at 1064 nm was employed as an output coupling mirror. The gain medium is an uncoated a-cut of 2% Nd:-YVO4.

The Gaussian beam ($HG_{0,0}$) generated by the hemi-cylindrical cavity was astigmatic due to the radii of the cylindrical front mirror [16]. Therefore, the beam divergence angle differed between horizontal (x–z) and vertical (y–z) directions. The transverse profile varied along the z-axis when the fundamental mode was utilized. However, by controlling off-axis pumping, the astigmatic fundamental mode can be transformed into high-order astigmatic HG modes.

Figure 2a illustrates the curve trend of the beam divergence in horizontal and vertical directions. The dashed and solid lines represent the beam divergence in the y–z and x–z planes, respectively. In addition, Fig. 2a1–a5 demonstrate the experimental patterns of the transverse astigmatic fundamental Gaussian beam along the z-axis where it can be seen that the intensity of the near-field differs from that of far field because of the different beam divergence in the y–z and x–z planes. As shown in Fig. 2a1–a2, although z remains between 0 and 35 mm, the intensity profile's shape appears to have expanded in the horizontal direction because the beam divergence of the x–z plane is greater than that of the y–z plane. Figure 2a3 shows that, when z is equal to 35 mm, the intensity profile exhibits a disk shape, mainly due to the similarities in the beam divergence of the x–z plane and the y–z plane. Figure 2a4–a5 demonstrate the intensity profile for $z > 35$ mm. The shape is limited to the vertical direction because the beam divergence of the y–z plane is greater than the x–z plane. Consequently, the beam divergence of the y–z plane increased faster than the x–z plane along the propagation direction. Therefore, the intensity profile varied from being horizontally stretched to being vertically stretched depending on the propagation distance. The Mathematica software program was used to analyze the intensity profile at $z = 35$ mm to verify whether the shape of the experimental laser mode was disk-shaped. Figure 2a6 presents the analysis result of Fig. 2a3, where the black and red curves represent the x- and y-directions of the image, respectively. The abscissa and ordinate delineate the position of the pattern and pixel intensity, respectively. According to the analysis results, the experimental transverse pattern for $z = 35$ mm was a disk-shaped experimental pattern.

The one-dimensional HG mode traveling through an arbitrary optical system of the ABCD matrix can be represented as

$$u_n(x,z) = \sqrt{\frac{\sqrt{2}}{2^n n!\omega_o\sqrt{\pi}}}\left(\frac{1}{A+\frac{B}{q_0}}\right)^{n+\frac{1}{2}}\left(\frac{\omega}{\omega_o}\right)^n \times H_n\left(\frac{\sqrt{2}x}{\omega}\right)\exp\left[-i\frac{\pi x^2}{\lambda q}\right], \tag{1}$$

where λ is the wavelength in free space, ω_o is the beam waist, ω is the spot size, $q_0$is the q parameter at the beam waist,$H_n(.)$is a Hermite polynomial of order n, $q = (Aq_0 + B)/(Cq_0 + D)$ and $\omega = \omega_o((A + B/q_0)^2 + i[2B\lambda(A + B/q_0)/\pi\omega_o^2])^{1/2}$. By considering the hemi-cylindrical cavity as an anisotropic two-dimensional system, the two-dimensional HG mode can be represented as

$$u_{n,m}(x,y,z) = u_n(x,z)\times u_m(y,z) = \sqrt{\frac{1}{2^{n+m-1}\pi n!m!\omega_{ox}\omega_{oy}}}\left(\frac{1}{A_x+\frac{B_x}{q_{0x}}}\right)^{n+\frac{1}{2}}\left(\frac{1}{A_y+\frac{B_y}{q_{0y}}}\right)^{m+\frac{1}{2}}\left(\frac{\omega_x}{\omega_{ox}}\right)^n\left(\frac{\omega_y}{\omega_{oy}}\right)^m \times H_n\left(\frac{\sqrt{2}x}{\omega_x}\right)H_m\left(\frac{\sqrt{2}y}{\omega_y}\right)\exp\left[-i\frac{\pi x^2}{\lambda q_x}\right]\exp\left[-i\frac{\pi y^2}{\lambda q_y}\right], \tag{2}$$

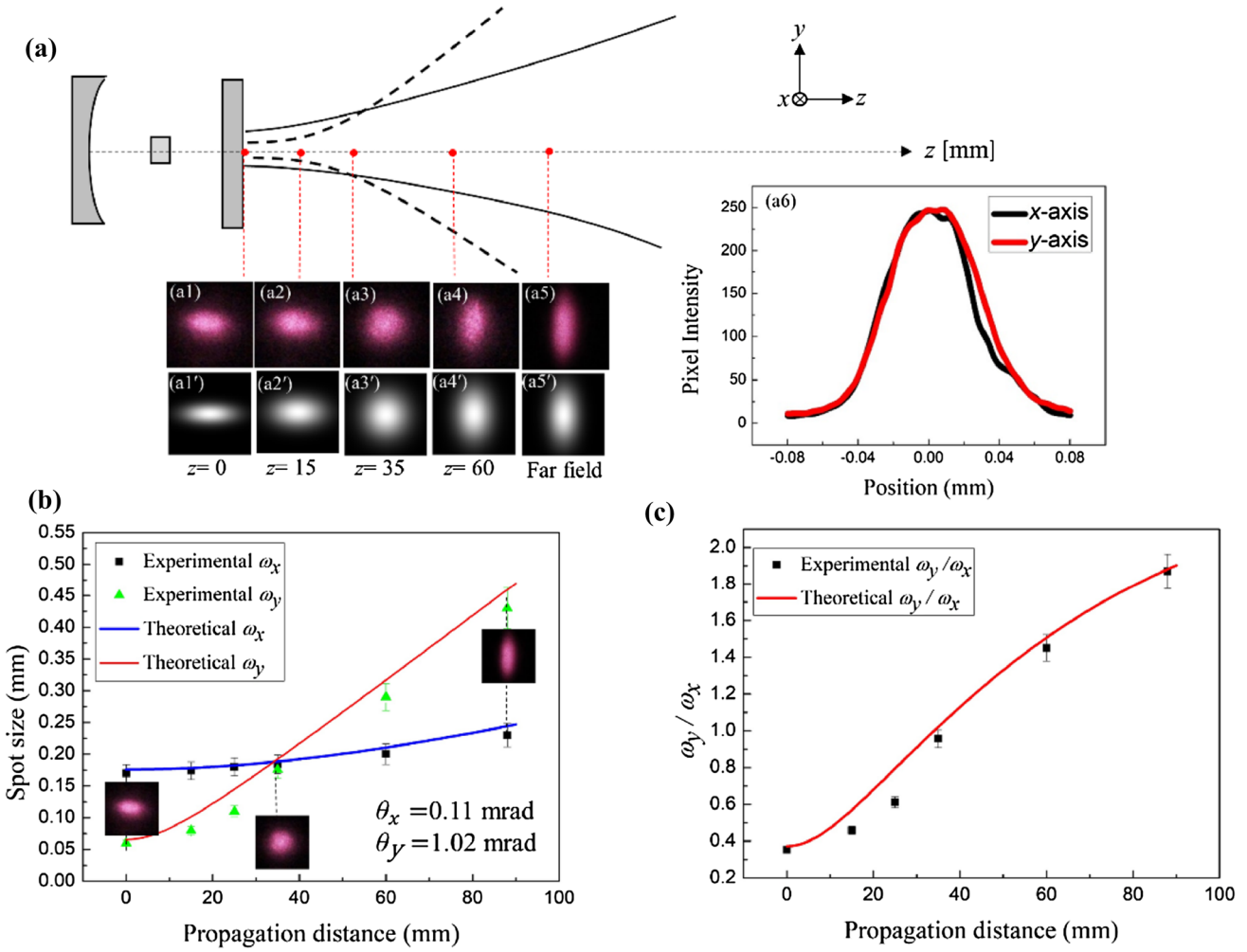

Fig. 2 **a** *a1–a5* Experimental transverse patterns of the astigmatic $HG_{0,0}$ mode from the near to far field, and it can correspond to the numerical transverse pattern of *a1′–a5′*. *a6* Software analysis result for *a3*. The black and red lines represent the spot size in the *x–z* and *y–z* planes, respectively. **b** Diagram of spot size–propagation distance without the extra-cavity cylindrical lens with an 8% error bar. The blue and red lines represent the theoretical values, and the data points represent the measured value, respectively. **c** Diagram of the ω_y/ω_x -propagation distance without an extra-cavity cylindrical lens with a 5% error bar. The red line and data points represent the theoretical and experimental values, respectively

where $\boldsymbol{\omega_{ox}} = [\lambda/\pi[L(R_x - L)]^{1/2}]^{1/2}$ and $\boldsymbol{\omega_{oy}} = [\lambda/\pi[L(R_y - L)]^{1/2}]^{1/2}$. The R_x and R_y represent the radius of the front cylindrical lens in *x*- and *y*-directions, respectively. In Eqs. (1) and (2), each element of ABCD matrix is related to propagation matrix. As an example, the propagation matrix for the laser mode emitted from hemi-cylindrical cavity can be represented as

$$M_x(z) = M_y(z) = \begin{pmatrix} 1 & z \\ 0 & 1 \end{pmatrix} = \begin{pmatrix} A & B \\ C & D \end{pmatrix}. \quad (3)$$

Substituting Eq. (3) into (2), $\boldsymbol{\omega_x}$ and $\boldsymbol{\omega_y}$ can be defined when the R_x and R_y is given. Therefore, Eq. (2) can be used to describe the theoretical spot sizes of the *x–z* (ω_x) and *y–z* planes (ω_y). Figure 2b represents the variation in the spot sizes of the *x–z* and *y–z* planes, which is generated from the hemi-cylindrical cavity for $R_x = 1200$ mm and $R_y = 30$ mm. The line and data points represent the theoretical and experimental values, respectively. The graph describes the magnitude of beam divergence in the *x–z* and *y–z* planes. We can observe an intersection of the two curves at a propagation distance of 35 mm, which represents the isotropic condition. The anisotropic conditions, meanwhile, can be observed before or after the intersection and the spot shape depends on the spot size. The *x–z* and *y–z* planes have divergence angles of 0.11 and 1.02 mrad, respectively. Figure 2c presents the ratio between ω_y and ω_x which increases along the propagation distance even up to distances beyond the scope of this study. The red line and data points represent the theoretical and experimental values, respectively. Thus,

the phenomena produced by the hemi-cylindrical cavity can be completely understood by comparing all the data points at the same propagation distance in Fig. 2b, c. Numerical experimental laser patterns were also calculated by Eq. (2), and there were shown in Fig. 1a1′–a5′.

The anisotropic $HG_{0,0}$ mode was transformed into the $LG_{0,0}$ mode by utilizing an extra-cavity cylindrical lens. The rotated HG mode can be expanded into a set of HG bases without rotation, and the rotated HG mode with the same axes as the extra-cavity cylindrical lens can be expressed as

$$u_{n,m}(x',y',z) = \sum_{s=0}^{N} d^{\frac{N}{2}}_{s-\frac{N}{2},n-\frac{N}{2}}(\theta) \times u_{s,N-s}(x,y,z), \tag{4}$$

where $x' = x\cos\theta + y\sin\theta$, $y' = x(-\sin\theta) + y\cos\theta$, $N = n + m$, and

$$d^{\frac{N}{2}}_{s-\frac{N}{2},n-\frac{N}{2}}(\theta) = \sqrt{s!}\sqrt{(N-s)!}\sqrt{n!}\sqrt{(N-n)!} \times \sum_{v=\max[0,s-n]}^{\min[N-n,s]} \frac{(-1)^v[\cos(\theta)]^{n+s-2v}[\sin(\theta)]^{m-s+2v}}{v!(N-n-v)!(s-v)!(n-s+v)!}. \tag{5}$$

Equation (5) is the weighting coefficient. Notably, the rotated angle of the extra-cavity cylindrical lens corresponds to θ. The ABCD matrix is revised because of the extra-cavity cylindrical lens, and it can be represented as

$$M_x(z) = \begin{pmatrix} 1 & z \\ 0 & 1 \end{pmatrix} \cdot \begin{pmatrix} 1 & 0 \\ 0 & 1 \end{pmatrix} \cdot \begin{pmatrix} 1 & d \\ 0 & 1 \end{pmatrix},$$
$$M_y(z) = \begin{pmatrix} 1 & z \\ 0 & 1 \end{pmatrix} \cdot \begin{pmatrix} 1 & 0 \\ -\frac{1}{f} & 1 \end{pmatrix} \cdot \begin{pmatrix} 1 & d \\ 0 & 1 \end{pmatrix} \tag{6}$$

where d is the distance between the hemi-cylindrical cavity and extra-cavity cylindrical lens, and f is the focal length of the extra-cavity cylindrical lens. By substituting Eq. (2) into (4), the optical field distribution of astigmatic HG modes traveling through an extra-cavity cylindrical lens with a rotation angle can be analyzed.

The beam divergence angle of the y–z modes is significantly higher than that in the x–z direction (Fig. 2) from the hemi-cylindrical cavity, as previously mentioned. Therefore, we placed an extra-cavity cylindrical lens with a focal length of 25 mm at a distance of 25 mm from the cavity to modify the beam divergence angle. The distance between output mirror and the extra-cavity cylindrical lens is a critical parameter for converting HG into LG, the shape of generated LG is like a disk-shape when the distance approaches the focal length of the extra-cavity cylindrical lens. The extra-cavity cylindrical lens exhibited the same structure as the front mirror, which had different curvature radii in the x- and y-axes. This suggested that the modification capabilities of the two axes were different. Therefore, the experimental laser mode generates the different shapes of the light beam due to the inserted extra-cavity cylindrical lens. When the angle of the extra-cavity cylindrical lens has been rotated, it affects the modified efficiency as well as ω_x and ω_y.

Figure 3a presents the experimental intensity patterns in the cavity with an extra-cavity cylindrical lens of $\theta = 66°$. Typically, the HG can be transformed into LG when $\theta = 45°$. The reason why $\theta = 66°$ is about the asymmetric thermal lens effect in this experiment. The shape of pump beam on the gain medium is changed by the asymmetric cylindrical front mirror. Therefore, it is a different condition when the symmetric spherical mirror is used as the front mirror [17]. Figure 3a2–a9 demonstrate that $\omega_x$and $\omega_y$were gradually modified along the propagation distance. As shown in Fig. 3a2–a5, although z remained between 25 and 300 mm, the field distribution was restricted at $\theta = 66°$ and ω_y was significantly modified along the propagation distance until it was approximately equal to ω_x. According to Fig. 3a6, the laser mode appeared disk-shaped, because ω_x was approximately the same as ω_y at $z = 300$ mm. Mathematica was used to confirm the shape of the intensity profile. Thus, it was ascertained that ω_x and ω_y are approximately the same, as illustrated in Fig. 3a10, indicating that the intensity profile is disk-shaped at $z = 300$ mm; the red and black curves in Fig. 3a10 represent ω_x and ω_y, respectively. However, ω_x and ω_y continuously changed its shape to $z > 300$ mm. Figure 3a7–a9 demonstrates that the pattern varied from a disk to ellipse shape. It varied more slowly for $z > 300$ mm, and achieved a stable experimental pattern in the far field. For example, the far field experimental pattern of Fig. 3a9 at $z = 5$ m has a very similar experimental pattern to those for $z = 700$ and 1000 mm. The theoretical ω_x and ω_y values were calculated to completely understand the whole field distribution along propagation distance. Figure 3b shows the diagram of the theoretical ratio of $\omega_y$and ω_x at $\theta = 66°$ with experimental data points; the theoretical component was calculated using Eq. (4). The black line and red points represent the theoretical and experimental ratios of ω_y and ω_x, respectively. The curve in Fig. 3b suggests that the modification was significant within the range of 25–300 mm and tended to stabilize afterward. Notably, the disk-shaped laser mode can be achieved if the ratio of ω_y and ω_x is approximately 1, which occurs when z is in the range of 200–300 mm. Figure 3b1–b5 illustrate the intensity profiles for different propagation distances and correspond to the numerical profiles of Fig. 3b1′–b5′. An error occurred in the rotated angle of the laser mode for $z > 400$ mm. There were some angle differences between the experimental intensity and the numerical profile. For this phenomenon, we think that it was caused by the complex asymmetric thermal lens effect which was generated by the cylindrical front mirror. All the aforementioned experimental phenomena can be explained by the theoretical graph presented in Fig. 3b.

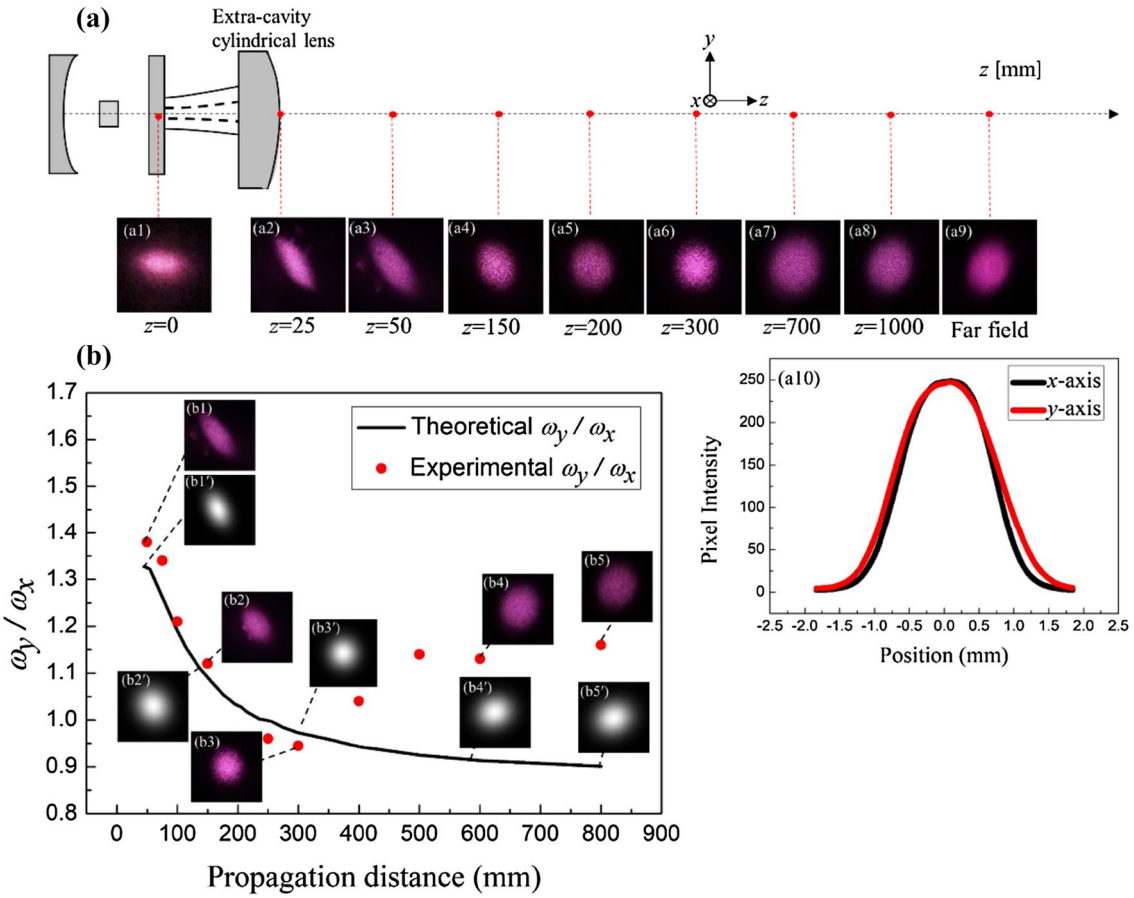

Fig. 3 **a** *a1–a9* Experimentally modified $HG_{0,0}$ modes at different propagation distances. *a10* Software analysis result for *a6*. Black and red lines represent spot sizes in *x–z* and *y–z* planes. **b** Diagram of the ratio of spot size and propagation distance for the extra-cavity cylindrical lens; the modification condition is also shown. The beam divergence is gradually modified. Black line and red data points represent theoretical and experimental ratios of ω_y and ω_x. *b1–b5* show experimental patterns at different propagation distances and correspond to the numerical patterns of *b1′–b5′*

Consequently, to understand how the extra-cavity cylindrical lens modified the spot size and beam divergence along the propagation distance, Fig. 3a, b, and Fig. 2 must be compared. For example, the ratio ω_y and ω_x was initially equal to 4 without the extra-cavity cylindrical lens, and it was modified to 0.8 by the extra-cavity cylindrical lens at $z = 800$ mm. Obtaining disk-shaped laser modes within the range of 200–300 mm indicated that we achieved a good quality LG mode by adjusting the off-axis pumping in this range.

3 The high-order laser modes generated from a hemi-cylindrical cavity with or without extra-cavity cylindrical lens

The astigmatic HG mode was generated by adjusting the off-axis pumping of the hemi-cylindrical cavity without the extra-cavity cylindrical lens. The high-order astigmatic HG modes were also influenced by the beam divergence angles in *x–z* and *y–z* planes. Therefore, these high-order astigmatic HG modes varied along the propagation direction. Figure 4a1–a5 show the experimental results for high-order astigmatic $HG_{0,5}$ along the propagation direction from the near to far field; these experimental patterns correspond to the numerical patterns of Fig. 4a1′–a5′ which are calculated using Eq. (2). The patterns exhibited a variation in the anisotropic HG mode and different structural variations compared with the traditional HG mode. The LG mode can be generated by the off-axis pumping of the hemi-cylindrical cavity with the extra-cavity cylindrical lens. The beam divergences of *x–z* and *y–z* planes were modified by the extra-cavity cylindrical lens, which was same as that in Fig. 3. Figure 4b1 indicates that the astigmatic $HG_{0,5}$ mode was generated from the hemi-cylindrical cavity. Figure 4b2–b4 show the variation of the experimentally modified LG modes along the *z*-axis; these experimental patterns correspond to the numerical patterns of Fig. 4b1′–b4′ which are calculated

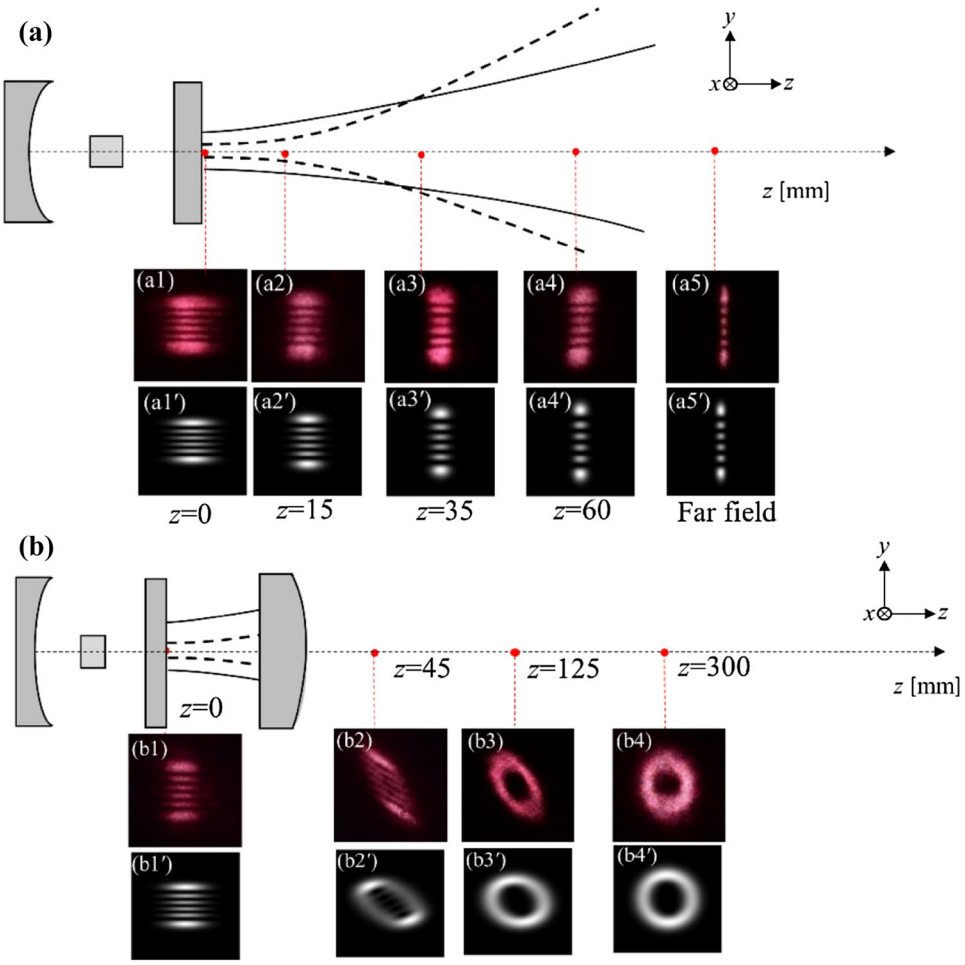

Fig. 4 **a** *a1–a5* Experimental transverse patterns of the astigmatic $HG_{0,5}$ mode from the near to far field generated by off-axis pumping, and these experimental patterns can correspond to numerical patterns of *a1′–a5′*. **b** *b1–b4* Experimental patterns of $HG_{0,5}$ mode under off-axis influence from the near to far field which can correspond to the numerical results of *b1′–b4′*. This setup transformed anisotropic HG modes into LG modes

using Eq. (4). As shown in Fig. 4b4, the LG mode is preferable because the spot sizes in each direction were approximately the same.

Figure 5 shows an extra-cavity cylindrical lens with an experimental laser mode for different rotation angles. We assumed that the angle θ is related to the y-axis of an extra-cavity cylindrical lens (the radius direction). The experimental pattern changes according to the rotation angle. Figure 5a–e show the experimental $HG_{0,0}$ mode at different rotation angles. At $\theta = 66°$, the experimental $HG_{0,0}$ mode

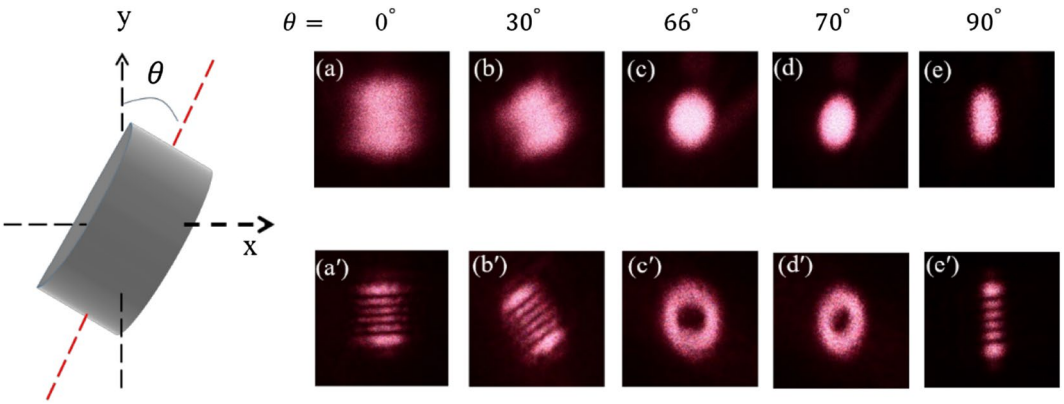

Fig. 5 *a–e* Experimental $HG_{0,0}$ modes with different angles of an extra-cavity cylindrical lens. *a′–e′* Experimental $HG_{0,5}$ modes with different angles of an extra-cavity cylindrical lens

was modified into an isotropic or disk-shaped Gaussian beam. This indicated that the hemi-cylindrical cavity and the rotation angle of the extra-cavity cylindrical lens were perfectly matched. To generate an LG mode, the rotation angle was fixed at 66°. Figure 5a′–e′ shows the experimentally modified high-order astigmatic $HG_{0,5}$ modes with off-axis pumping. The LG mode was successfully generated at the rotation angle of 66°.

4 Analyses of a hemi-cylindrical cavity with an extra-cavity cylindrical lens

As illustrated in Figs. 2, 3, 4 and 5, an extra-cavity cylindrical lens was not only used to modify the beam divergence angle but also to adjust the off-axis pumping and specific angle of the extra-cavity cylindrical lens to generate the LG modes.

4.1 Relationship between the cavity length and angle of extra-cavity cylindrical lens

The beam divergence angles of lasers vary with cavity lengths. In here, each beam divergence angle, corresponding to a certain cavity length, was matched to a specific extra-cavity cylindrical lens angle to generate LG modes. Figure 6 indicates that different cavity lengths can correspond to perfect angles of the extra-cavity cylindrical lens. For example, Fig. 5c′ depicts the LG mode for a cavity length of 7 mm and angle of 66° in the extra-cavity cylindrical lens.

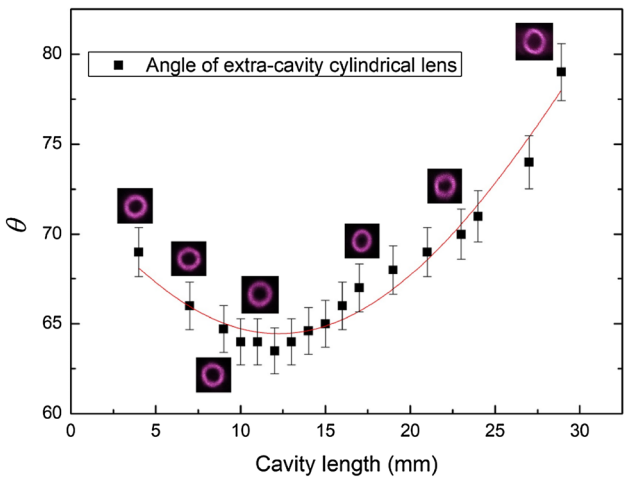

Fig. 6 Angle of the extra-cavity cylindrical lens versus cavity lengths with a 2% error bar. Cavity lengths correspond to angles of the extra-cavity cylindrical lens to generate the LG mode

4.2 Relationship between cavity length and power

The laser cavity length played an important role in this experiment. The patterns had different beam divergence angles and mode sizes at different cavity lengths. In general, the orders of the HG and LG modes increased when the mode size decreased, as determined by the ratio of pump and mode sizes [18]. We usually adjust the cavity length to change the mode size. Figure 7 shows the power versus off-axis pumping curves for cavity lengths of 7 and 10 mm. The output power was low because a pumping source of 2W was used. Also, the lower output power was caused by the large cavity loss which was generated from the hemi-cylindrical cavity. The curve decreased when the off-axis pumping increased. Moreover, the shorter cavity length exhibited higher order laser modes. This also implied that the mode size of the 7 mm cavity is smaller than the 10 mm cavity. Consequently, the order of the LG mode was proportional to the off-pumping axis, and the power of the pattern was inversely proportional to the order of the pattern in this experiment.

5 Conclusion

The hemi-cylindrical cavity produced the laser mode that has different beam divergence angles in the x–z and y–z planes from the near to far field. To modify the beam divergence angles, an extra-cavity cylindrical lens is required. The extra-cavity cylindrical lens either modifies the anisotropic fundamental mode to isotropic fundamental mode in a specific range or generates LG mode under an off-axis pumping influence. The theoretical curve of the hemi-cylindrical

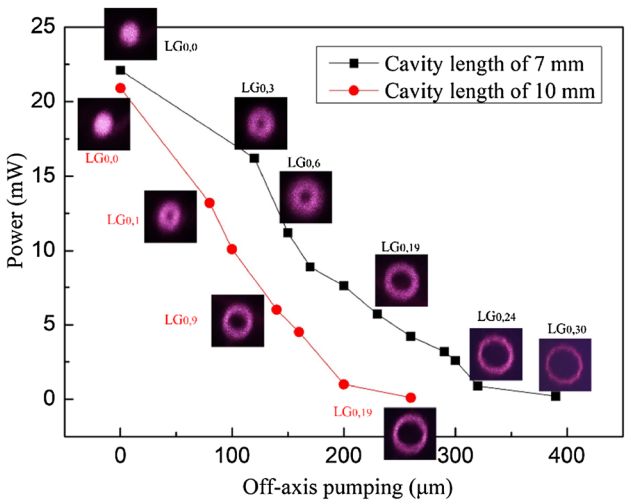

Fig. 7 Power versus off-axis pumping curves for cavity lengths of 7 mm (black line) and 10 mm (red line)

cavity with or without an extra-cylindrical lens is consistent with the experimental results at each propagation distance. The LG modes can be generated by a hemi-cylindrical cavity with an extra-cavity cylindrical lens, and these can be produced using different cavity lengths each corresponding to a specific extra-cavity cylindrical lens angle. Furthermore, the order of the LG mode was proportional to the off-axis pumping. All of the experimental results can be verified by the quantitative analysis in this paper.

Acknowledgements The authors thank the Ministry of Science and Technology for their financial support of this research under Contract No. MOST 106-2112-M-003-011.

References

1. L. Allen, M.W. Beijersbergen, R.J. Spreeuw, J.P. Woerdman, Phys. Rev. A **45**, 8185 (1992)
2. N.B. Simpson, L. Allen, M.J. Padgett, J. Mod. Opt. **43**, 2385 (1996)
3. A. Lafong, W.J. Hossack, J. Arlt, Opt. Express **14**, 3065 (2006)
4. G. Millione, T.A. Nguyen, J. Leach, D.A. Nolan, R.R. Alfano, Opt. Lett **40**, 4887 (2015)
5. P. Senthilkumaran, Appl. Opt. **42**, 6314 (2003)
6. A. Mair, A. Vaziri, G. Weihs, A. Zeilinger, Nature **412**, 313 (2001)
7. K. Dholakia, N.B. Simpson, M.J. Padgett, Phys. Rev. A **54**, R3742 (1996)
8. M.W. Beijersbergen, L. Allen, and J.P. Woerdman, H.E.L.O. van der Veen. Opt. Commun. **96**, 123 (1993)
9. K. Sueda, G. Miyaji, N. Miyanaga, M. Nakatsuka, Opt. Express **12**, 3548 (2004)
10. L. Marrucci, C. Manzo, D. Paparo, Phys. Rev. Lett. **96**, 163905 (2006)
11. J. Arlt, K. Dholakia, L. Allen, M.J. Padgett, J. Mod. Opt. **45**, 1231 (1998)
12. N. Matsumoto, T. Ando, T. Inoue, Y. Ohtake, N. Fukuchi, T. Hara, J. Opt. Soc. Am. **25**, 1642 (2008)
13. Y.F. Chen, Y.P. Lan, S.C. Wang, Appl. Phys. B. **72**, 167 (2001)
14. T.H. Lu, Y.C. Lin, Y.F. Chen, K.F. Huang, Appl. Phys. B **103**, 991 (2011)
15. T.H. Lu, Y.C. Wu, Opt. Express **21**, 28496 (2013)
16. J.A. Arnaud, H. Kogelnik, Appl. Opt. **8**, 1687 (1969)
17. Y.F. Chen, C.C. Chang, C.Y. Lee, J.C. Tung, H.C. Liang, K.F. Huang, Laser Phys. **28**, 015002 (2018)
18. Y.F. Chen, J. Opt. Soc. Am. **17**, 1835 (2000)